Design and Fabrication of TiO2/Lignocellulosic Carbon Materials

Accepted Article

Title: Design and fabrication of TiO2/lignocellulosic carbon materials: relevance of low-temperature sonocrystallization to photocatalysts performance

Authors: Juan Carlos Colmenares, Paweł Lisowski, Ondřej Mašek, Wojciech Lisowski, Dmytro Lisovytskiy, Justyna Grzonka, and Krzysztof Kurzydłowski

FULL PAPER WILEY-VCH

Design and fabrication of TiO₂/lignocellulosic carbon materials: relevance of low-temperature sonocrystallization to photocatalysts performance

Paweł Lisowski,*[a] Juan Carlos Colmenares,*[a] Ondřej Mašek,[b] Wojciech Lisowski,[a] Dmytro Lisovytskiy,[a] Justyna Grzonka,[c, d] and Krzysztof Kurzydłowski[c]

We present a facile and green approach to produce crystalline TiO₂ nanoparticles on a surface of different carbonaceous materials derived from lignocellulosic biomass such as STARBON-800® obtained by carbonization at 800 °C and biochar-SWP700 (Soft Wood Pellets (SWP) obtained by pyrolysis at 700 °C) *via* novel low-temperature ultrasound-promoted green methodology coupled with citric acid as a cross-linking agent. In comparison to other methods, the developed method has several significant benefits such as simplicity, great ability to get crystalline TiO₂ particles (elimination of high-temperature treatment (material calcination at > 300 °C) needed in the conventional sol-gel method, which is extremely important in transforming amorphous TiO₂ into a photoactive crystalline phase) elimination of risky chemicals and oxidizing agent, and also ability to change some parameters (e.g. ultrasound intensity). Prepared materials were characterized by XRD, DR UV–vis, N₂ physisorption, HR-XPS, XRF, HR-TEM, FT-IR and subsequently tested for their photocatalytic activities both in photocatalytic phenol degradation (in water) and oxidation of methanol (in air) under UV and visible light irradiation.

Introduction

In recent years, development of green and low environmental-impact technologies combined with renewable resources through innovation can offer alternatives to potentially useful processes for a more sustainable carbon-based society.[1] The synergistic effects of coupling TiO₂ with carbon materials bearing enhanced multi-functionalities for use in heterogeneous photocatalysis, energy-storage, and solar cell applications, renders TiO₂ immobilized on porous carbon as a valuable material.[1] From a practical point of view, alternative photocatalytic materials that can match the TiO₂ profile, namely versatility, inexpensiveness and abundance, and a non-toxic nature are hard to find.[1, 2]

Elegant strategy for preparation of porous carbon materials derived from biomass (e.g. starch) was developed and patented by Clark et al.[3] from the Green Chemistry Centre of Excellence, (University of York, UK) and classified under the trademark "STARBON®". These new materials are mechanically and thermally very stable (200-1000 °C), possess graphitic-like surface (> 700 °C), high mesoporosity (V_{meso}>0.3 cm³ g⁻¹) and high specific surface areas (S_{BET}>500 m² g⁻¹).[3] On the other hand, biochar is a newly developed C-enriched material derived from biomass by thermochemical treatment under moderate temperature (e.g. 350–700 °C) in a reactor at oxygen-limited supply conditions.[4] An important advantage of Starbon and biochar over more conventional activated carbon is the presence of abundant surface functional groups (e.g., phenolic hydroxyl, carbonyl, and carboxyl groups). These new carbon materials like "Starbons" and biochar offer for tremendous photocatalysis potential due to their various functional surface[4] to prepare new inorganic-organic composite photoactive materials.

The phenomenology of fabrication of highly efficient photocatalysts through ultrasound-based procedures may offer a new tool, and it holds great potential in the near future for photocatalysts preparation.[5] In comparison with traditional sources of energy, sonication ensures unusual reaction conditions in liquid phase reactions due to the cavitation phenomenon (cavitational collapse produces intense local heating (hot spots of ~5000 °C), extreme pressures (~1000 bar), and rapid heating/cooling rates (10^{10} °C s⁻¹)), thus a large number of catalyst preparation can be carried out in shorter reaction time, milder and greener conditions under ultrasound exposure compared to conventional methods.[5, 6] Ultrasound may also help in controlling the course of rapid crystallization processes ("sonocrystallization") in which the nuclei are produced due to cavitation process, and ultrasound can control crystal size distribution and reduces the particle agglomeration resulting in more stable particles.[6] The introduction of ultrasound in sol-gel reactions has rapidly attracted the attention of researchers, and nowadays ultrasound effects on the heterogeneous systems are an essential tool for industrial applications.[6, 7] Neppolian et al.[8] prepared nano-size TiO₂ photocatalysts by sol-gel and ultrasonic-assisted sol-gel methods using two different sources of ultrasound, i.e., a bath type and tip type, with the final material calcination at 500 °C for 3 h. Recently Eskandarloo et al.[9] synthesized pure TiO₂ and samarium, cerium mono-doped and co-doped TiO₂ catalysts by an ultrasonic-assisted sol-gel method and calcination at 450 °C for 3 h. Prasad et al.[10] synthesized TiO₂ by ultrasound-assisted sol-gel technique and material calcination at 750 °C for 3 h. Pinjari et al.[11] synthesized TiO₂ using both conventional and ultrasound-assisted sol-gel technique. The experiments were conducted at a constant calcination temperature of 750 °C and the calcination time was varied from 30 min to 3 h. As it is observed in the open literature, the combination of ultrasound with sol-gel always demanded a final high-temperature calcination step.

Among all polycarboxylic acids, citric acid (CA) with multi-carboxylic functional structure is a prospective candidate as the best additive in several nanomaterial syntheses due to their natural origin, broad availability and cost-effectiveness.

[a] M.Sc. P. Lisowski, Professor J. C. Colmenares, Ph.D. W. Lisowski, Ph.D. D. Lisovytskiy
Institute of Physical Chemistry, Polish Academy of Sciences, Kasprzaka 44/52, 01-224 Warsaw, Poland
E-mail: plisowski@ichf.edu.pl, jcarloscolmenares@ichf.edu.pl, (http://photo-catalysis.org)
[b] Ph.D. Ondřej Mašek
UK Biochar Research Centre, School of Geosciences, University of Edinburgh, Edinburgh, UK, (UKBRC)
[c] Ph.D. J. Grzonka, Professor K. Kurzydłowski
Faculty of Materials Science and Engineering, Warsaw University of Technology, Woloska 141, 02-507 Warsaw, Poland
[d] Ph.D. J. Grzonka
Institute of Electronic Materials Technology, Wolczynska 133, 01-919 Warsaw, Poland

Additionally, citric acid has been studied as an "eco-friendly" non-formaldehyde cross-linking agent to improve the physical-chemical properties (bearing hydroxyl and carboxyl groups) of lignocellulosic carbon materials derived from biomass such as chitosan,[12] silk,[13] wool,[14] starch,[15] cashew gum (polysaccharide from natural sources),[16] cotton,[17] cellulose,[18] wood[19] and paper.[20] Citric acid has three carboxyl (–COOH) and one hydroxyl (–OH) groups, which have the possibility to react with two or more of the hydroxyl groups present in abovementioned biomass-based polymers and ether- or/and esterification could take place between the carboxyl groups of CA and the hydroxyl groups of those biopolymers and can be expected to cross-link and improve their properties. Citric acid can also be used as stabilizing coordination agent sol-gel method as a, which may significantly inhibiting metal ions segregation and making the precursor homogeneous.[12-20] It was established that citric acid is an excellent chelating agent and a suitable precursor that ensures high specific surface area and nanometric particle size.[21] Yin et al.[22] produced 2-10 nm crystallites of the monodispersed phase of pure anatase by using citric acid to stabilize the TiO_2 nanoparticles and promote the nucleation for anatase phase formation during a hydrothermal procedure. Montazer et al.[14 c] applied wool fabrics along with citric acid (CA) as a crosslinking agent to stabilize the TiO_2/Ag nanoparticles on the wool surface. On the other hand, other research has found that citric acid can reduce the crystallization temperature of yttrium orthoferrite (from 850 to 400 °C).[23]

We have developed a series of novel crystalline TiO_2 supported on lignocellulosic carbon materials prepared via ultrasound-assisted sol-gel method. The photocatalytic activity of these materials was tested in the photocatalytic oxidation of methanol in the gas phase and phenol photodegradation in aqueous phase under UV and visible light irradiation. In comparison to other methods, the developed method has a lot of significant advantages such as simplicity, cost-effectiveness, great ability to obtain crystalline TiO_2 particles of reproducible size, easy to perform at mild conditions of temperature and pressure, elimination of hazardous chemicals and oxidizing agents, and also ability to play with some parameters (see SI, Fig. S1-S11). To the best of our knowledge, this is the first study on the production of crystalline TiO_2 nanoparticles on a surface of different carbonaceous material derived from lignocellulosic biomass using novel low-temperature ultrasonic-assisted sol-gel method coupled with citric acid as a cross-linking agent.

Results and Discussion

Brunauer–Emmett–Teller (BET) specific surface area analysis

The N_2 adsorption-desorption isotherms of all prepared materials are presented in Fig. 1. According to IUPAC classification, 20.4 wt. %TiO_2/SWP700_48 μm, 20.4 wt.% TiO_2/STARBON-800_48 μm and 20.4 wt. %TiO_2/NORIT_48 μm reveals that adsorption-desorption isotherms (Fig. 1) are of type IV/V, which is a feature of the mesoporous material structure.[24]
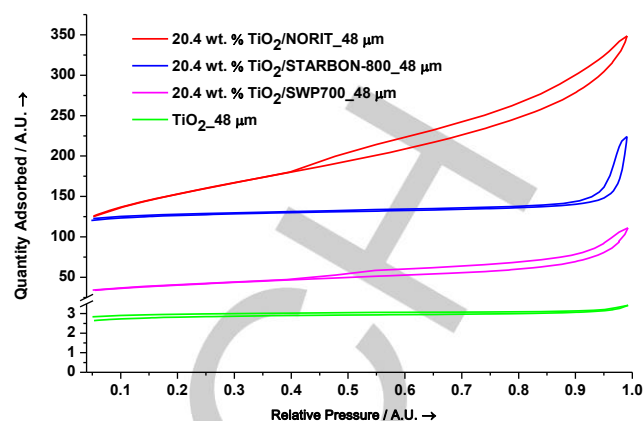

Figure 1. Nitrogen adsorption-desorption isotherms over all prepared materials

It should be emphasized that 20.4 wt. %TiO_2/STARBON-800_48 μm photocatalyst exhibits a significantly high surface area and pore volume as a result of well-developed mesoporosity (D = 17 nm) and very high V_{meso}/V_{tot} ratio (0.76) compared to the other materials with the same TiO_2 content (Table 1). It is also worth noting that comparing the specific surface area of composite materials prepared without ultrasound and without citric acid with materials prepared by means of ultrasound, together with the addition of citric acid may be stated that results showed an important effect of sonication on the textural properties. The use of ultrasound and citric acid during synthesis causes an increase of specific surface area together with V_{meso}/V_{tot} ratio in all prepared materials. In the case of TiO_2_48 μm, there was no characteristic hysteresis loop compared with composites. As can be seen from Table 1, the highest mesoporosity (0.76) is obtained for 20.4 wt. % TiO_2/STARBON-800_48 μm prepared by the ultrasound-induced sol-gel method. Additionally, the higher specific surface area of prepared materials may be ascribed to the effect of ultrasonic irradiation because it can produce cracks and increase the mesoporous structure of the 20.4 wt. %TiO_2/STARBON-800_48 μm. Furthermore, the high specific surface area was likely to increase the formation of more surface active sites demonstrating greater photocatalytic activity. It is well known that mesoporous structure allows light to scatter inside their pore channel, thus enhancing the harvesting of light.[25] It is also worth noting that the presence of mesoporous structure accelerates the nucleation rate for the formation of cavitation bubbles, producing superior cavitation effects to the nonporous material because pore corners in porous material can provide energetically preferred binding sites at which the new phase can be more easily held.[26]

Table 1. Results of BET specific surface area and t-plot analysis for all prepared materials

PhotoCatalyst	S_{BET} (m^2g^{-1})	S_{micro} (m^2g^{-1})	V_{micro} (cm^3g^{-1})	V_{tot} (cm^3g^{-1})	V_{meso} (cm^3g^{-1})	D (nm)	V_{meso}/V_{tot}
20.4 wt. %TiO_2/SWP700_48 μm	242	93	0.16	0.32	0.16	4	0.50
20.4 wt. %TiO_2/SWP700 without US+CA	135	74	0.17	0.20	0.03	3	0.15
20.4 wt. %TiO_2/SWP700_48 μm_without CA	199	86	0.21	0.29	0.08	3	0.28
20.4 wt. %TiO_2/STARBON-800_48 μm	517	205	0.12	0.50	0.38	17	0.76
20.4 wt. %TiO_2/STARBON-800 without US+CA	305	159	0.24	0.35	0.11	10	0.31
20.4 wt. %TiO_2/STARBON-800 48 μm_without CA	411	189	0.19	0.41	0.22	13	0.54
20.4 wt. %TiO_2/NORIT_48 μm	392	157	0.10	0.16	0.06	4	0.38
20.4 wt. %TiO_2/NORIT without US+CA	255	142	0.11	0.12	0.01	2	0.08
20.4 wt. %TiO_2/NORIT 48 μm_without CA	298	159	0.10	0.13	0.03	4	0.23
TiO_2_48 μm	22	20	0.05	0.06	0.01	2	0.17

X-ray diffraction (XRD)

In order to determine the crystal structure of all tested photocatalysts, X-ray powder diffraction experiment was carried out. XRD patterns compiled in Fig. 2 pointed out the clear presence of a distinctive TiO_2 anatase phase in 20.4 wt. % TiO_2/SWP700_48 μm (7 nm crystallite size) and 20.4 wt. % TiO_2/STARBON-800_48 μm (6 nm crystallite size) (Table 2). XRD pattern for 20.4 wt. %TiO_2/NORIT_48 μm reveals two small peaks at 2θ = ~22° and 2θ = ~26.6° that can be attributed to amorphous SiO_2.[27] As it is observed from Fig. 2, the XRD pattern of TiO_2_48 μm determines the amorphous structure (Table 2).
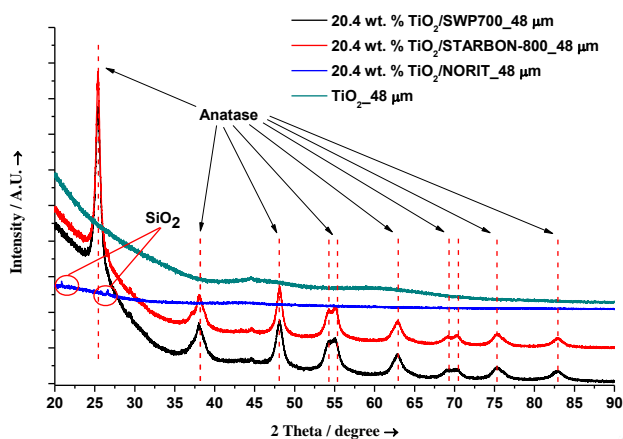

Figure 2. X-ray diffraction (XRD) pattern for all prepared photocatalysts

Table 2. Summary of the structural and optical features of the photocatalysts (nd = not detectable)

Photocatalyst	XRD		UV-Vis	
	Crystallite size (nm)	Crystal phase	E_{gap} (eV)	Absorption threshold (nm)
20.4 wt. %TiO_2/SWP700_48 μm	7	Anatase	2.71	459
20.4 wt. %TiO_2/STARBON-800_48 μm	6	Anatase	2.73	453
20.4 wt. %TiO_2/NORIT_48 μm	Amorphous	nd	nd	nd
TiO_2_48 μm	Amorphous	nd	3.38	368

UV−vis diffuse reflectance spectroscopy

UV-vis diffuse reflectance spectroscopy was employed to investigate the optical properties of all prepared materials. As illustrated in Fig. 3, 20.4 wt. %TiO_2/SWP700_48 μm and 20.4 wt. %TiO_2/STARBON-800_48 μm showed a wider photoabsorption from UV light to visible light with an absorption edge at around 459 nm and 453 nm, respectively (Table 2). Furthermore, the band gap energies of all prepared materials were estimated by Kubelka-Munk function (Fig. 4) and were found to be 3.38 eV for TiO_2_48 μm, 2.73 eV for 20.4 wt. % TiO_2/STARBON-800_48 μm and 2.71 eV for 20.4 wt. % TiO_2/SWP700_48 μm (Table 2). The shape of the DR UV-vis that optical band gap of TiO_2_48 μm for amorphous TiO_2 being in the range 3.30–3.5 eV,[28] which is higher than the value for single standard crystal anatase (3.20 eV). The progressive lowering of the band gap in the case of 20.4 wt. % TiO_2/STARBON-800_48 μm and 20.4 wt. %TiO_2/SWP700_48 μm may be attributed to the development of titania crystallinity during the composites synthesis as the composite material is prepared by ultrasound-assisted sol-gel method and the

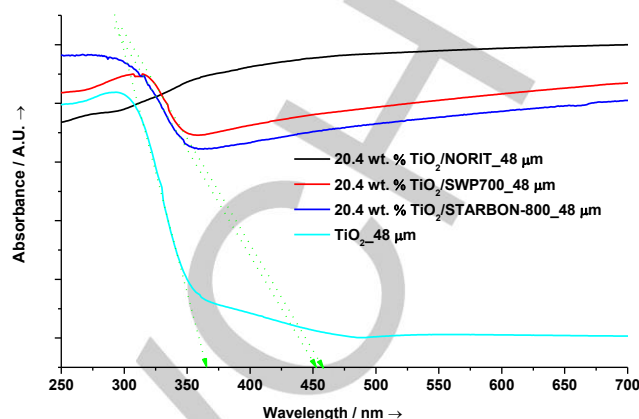associated evolution of surface defects such as oxygen vacancies during their preparation.

Figure 3. Diffuse reflectance UV-visible spectra of all prepared photocatalysts: 20.4 wt. %TiO_2/SWP700_48 μm ("red line"), 20.4 wt. %TiO_2/NORIT_48 μm ("black line"), 20.4 wt. %TiO_2/STARBON-800_48 μm ("blue line") and TiO_2_48 μm ("turquoise line")
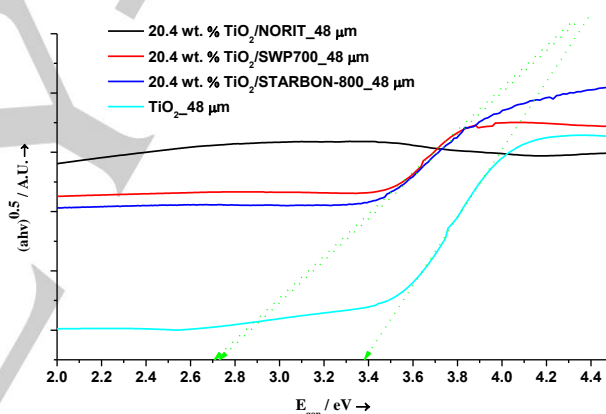

Figure 4. The plot of the transformed Kubelka–Munk function versus the energy of light for the calculation of E_{gap}

Additionally, very high Ti^{3+} in 20.4 wt. %TiO_2/STARBON-800_48 μm and 20.4 wt. %TiO_2/SWP700_48 μm (see SI, Table S2) can improve the transfer efficiency of electrons between lignocellulosic carbon materials and TiO_2, which will enhance the photocatalytic redox reactions (Ti^{4+} to Ti^{3+}).[29] The presence of Ti^{3+} and oxygen vacancy sites in the aforementioned composites can contribute to the visible-light absorption because of the formation of Ti^{3+} ions in the bandgap just below the conduction band (CB) of TiO_2, and the overlap between the oxygen defect states and titania CB states leads to a band gap decrease,[29] which results in the synthesized composites responsive to the visible light.

High-resolution X-ray photoelectron spectroscopy (HR-XPS)

To further obtain evidence about the plausible mechanism of interaction between carbon material surface and TiO_2 in the prepared TiO_2/carbon materials, HR-XPS analysis was carried out (see SI, Table S2). In all prepared composites the dominant bands of Ti 2p are located at binding energies of 460.9±0.2 eV

and 459.8 ±0.1 eV and clearly corresponds to Ti^{4+} and Ti^{3+} in TiO_2 structure.[29] In the case of 20.4 wt. %TiO_2/NORIT_48 μm composite there is no presence of the Ti^{3+} surface functional group. Furthermore, 20.4 wt. %TiO_2/STARBON-800_48 μm and 20.4 wt. %TiO_2/SWP700_48 μm exhibited very high atomic surface concentration (0.94 and 0.89 at. % respectively) of Ti^{3+} and very high sp^2/sp^3 ratio (1.48 and 4.85 respectively) compared with 20.4 wt. %TiO_2/NORIT_48 μm (1.01). It is worth mentioning that the O/Ti ratios for 20.4 wt. %TiO_2/STARBON-800_48 μm and 20.4 wt. %TiO_2/SWP700_48 μm composites are slightly below (1.96 in both cases) the stoichiometric value (O/Ti =2.0). Based on these results, it is expected for these composites the presence of a certain number of surface defects such as oxygen vacancies. In principle, the formation of oxygen vacancies on 20.4 wt. %TiO_2/STARBON-800_48 μm and 20.4 wt. %TiO_2/SWP700_48 μm may lead to the creation of unpaired electrons or Ti^{3+} centers to keep the charge balance. Suriye et al.[30] reported that TiO_2 surface defects (Ti^{3+}) play a significant role as they are active sites for oxygen adsorption and for trapping the electron to prevent the recombination of electrons and holes. Several authors also reported that surface Ti^{3+} sites provide the unique activity and selectivity in the target reactions[31] and can act as the retarding recombination center of light-excited electrons and holes.[32] Therefore, the increasing Ti^{3+} density promotes effective segregation of electrons, interface charge transfer, and then increases the photocatalytic performance.[29] The strong bands at 530.8 eV±0.2 eV and 529.9 eV±0.3 eV are corresponding to the Ti–O and Ti-O-Ti bonds of TiO_2, which means that the chemical state of oxygen is main lattice oxygen in titania.[33] The band at 532.4eV ±0.2eV is assigned to O–H bond (hydroxyl group), and water molecules adsorbed on the surface TiO_2.[34] The peak around 281 eV resulting from Ti–C bond was not observed, so carbon elements do not substitute oxygen atom in the lattice of anatase.[34]

High-resolution transmission electron microscopy (HR-TEM)

HR-TEM was used to further investigate the surface structure and morphology of 20.4 wt. %TiO_2/STARBON-800_48 μm and 20.4 wt. %TiO_2/SWP700_48 μm (Fig. 5). This analysis revealed that the prepared composites exhibited crystalline structures with tiny spherical nanoparticles of TiO_2, around 8-10 nm in size for 20.4 wt. %TiO_2/SWP700_48 μm and 20.4 wt. % TiO_2/STARBON-800_48 μm corresponds to the characteristic peaks of the TiO_2 anatase phase.
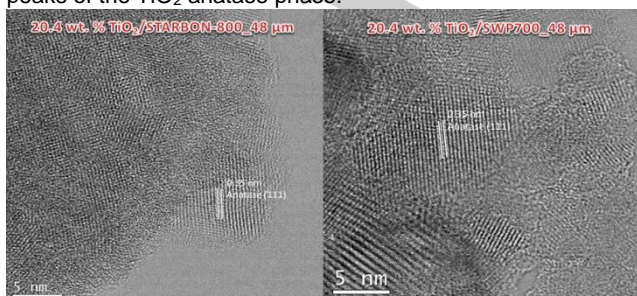
Figure 5. HR-TEM micrographs of 20.4 wt. %TiO_2/STARBON-800_48 μm and 20.4 wt. %TiO_2/SWP700_48 μm

Photocatalysts activities in aqueous phase

To evaluate the photocatalytic activity of all prepared TiO_2/carbon materials, photocatalytic phenol degradation was carried out under UV and visible irradiation after 240 min of irradiation (experimental details in SI). Furthermore, the prepared materials were tested at different % TiO_2 loading and at different ultrasound amplitudes (see SI, Fig. S6-S9) for TiO_2/STARBON-800 and TiO_2/SWP700. It needs to be highlighted that the best ultrasound amplitude used during the synthesis was 48 μm with pulse mode and the best loading of TiO_2 used during the synthesis was 20.4 wt. %TiO_2 for TiO_2/STARBON-800 and TiO_2/SWP700. No appreciable phenol degradation was found in the absence of UV and visible irradiation or catalyst. Moreover, the highest phenol degradation (UV light: 44.3 %, visible light: 17.7 %) was achieved with 20.4 wt. %TiO_2/STARBON-800_48 μm composite and a slightly lower percentage of degradation was achieved by 20.4 wt. % TiO_2/SWP700_48 μm (UV light: 42.7 %, visible light: 15.6 %) after 240 min. of irradiation (Fig. 6).
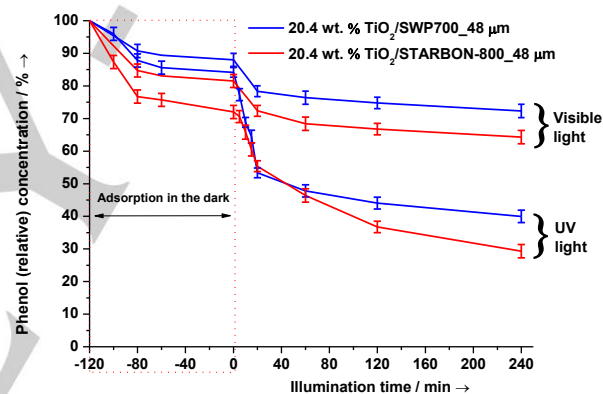
Figure 6. Photocatalytic phenol degradation under UV and visible light for TiO_2/STARBON-800_48 μm and TiO_2/SWP700_48 μm after optimization (error bars showing mean deviation of three experimental results)

In terms of adsorption properties in the dark, after 120 min. (Fig. 6) 20.4 wt. %TiO_2/STARBON-800_48 μm exhibited the highest surface adsorption of phenol (UV-based system: 24.7 %, visible-based system: 18.4 %) and 20.4 wt. %TiO_2/SWP700_48 μm (UV-based system: 15.8 %, visible-based system: 11.9 %) which is in good agreement with high specific surface area of prepared composites (517 m^2 g^{-1} and 242 m^2 g^{-1}, respectively) and highly mesoporous-based textural properties of 20.4 wt. % TiO_2/STARBON-800_48 μm. It is worth mentioning that the most active photocatalysts (20.4 wt. %TiO_2/STARBON-800_48 μm and 20.4 wt. %TiO_2/SWP700_48 μm) after 720 minutes of irradiation gave 53.3 % and 50.6 %, respectively (UV light), and 28.1 % and 24.9 %, respectively (visible light) phenol degradation in water.

X-Ray Fluorescence (XRF)

One important thing to highlight is the fact that titanium leaching after the photocatalytic tests was not observed in the

aqueous solution (confirmed by XRF analysis, see SI, Figure S12) for the best performing 20.4 wt. %TiO_2/STARBON-800_48 µm and 20.4 wt. %TiO_2/SWP700_48 µm photocatalysts prepared by ultrasound-assisted sol-gel method. The presence of trace elements observed in Figure S12 (fingerprints, very common) such as Rh, Fe, Cu is caused by X-ray source scatter.

Long-term stability test

Evaluation of photocatalysts reusability is necessary for their practical applications in water treatment by heterogeneous photocatalytic processes. To evaluate the long-term performance of the composite photocatalyst, a recycling test for phenol degradation was carried out. After each cycle, the photocatalyst was filtered out and left to dry at 110 °C overnight before use in the next cycle. As far as photocatalyst stability is concerned, our best photocatalytic materials (20.4 wt. % TiO_2/STARBON-800_48 µm and 20.4 wt. %TiO_2/SWP700_48 µm) were reused five times (Fig. 7) under the same reaction conditions with the loss of only < 6 % of phenol degradation after run 5. The results revealed that the photocatalytic activity of 20.4 wt. %TiO_2/STARBON-800_48 µm and 20.4 wt. % TiO_2/SWP700_48 µm photocatalysts exhibit excellent stability. Therefore, the prepared photocatalysts with promising activity and stability can be potential candidates for future practical applications.

Figure 7. Multi-cycle performance of 20.4 wt. %TiO_2/STARBON-800_48 µm and 20.4 wt. %TiO_2/SWP700_48 µm photocatalysts in degradation of phenol in aqueous

Photocatalytic activity in gas phase

First of all (more experimental details in SI), two control experiments were applied: (1) upon UV illumination in the presence of methanol in the air flow, without photocatalyst and (2) in the dark, in the presence of photocatalyst, methanol in the air flow and at the temperature up to 100 °C (the results of these experiments are not presented here). In the photolysis experiment (absence of photocatalyst), very low conversion of methanol (~5%) was observed, thus confirming that the reaction is indeed enabled by a photocatalytic process. In the second

experiment, thermal test up to 100 °C, 20.4 wt. % TiO_2/STARBON-800_48 µm and 20.4 wt. %TiO_2/SWP700_48 µm photocatalysts were not active. It should be also noted that, GC on-line analysis did not show any leaching of carbon (SWP700 and STARBON-800) during the photocatalytic test in gas phase for the best performing 20.4 wt. %TiO_2/STARBON-800_48 µm and 20.4 wt. %TiO_2/SWP700_48 µm photocatalysts (stability test: pure air flow (25 cm^3 min^{-1}), UV illumination and absence of methanol). Fig. S10-S11 (see SI) show the results of photocatalytic oxidation of methanol in gas phase at different ultrasound amplitudes and at different % TiO_2 loading for TiO_2/STARBON-800 and TiO_2/SWP700. Additionally, none of the pure SWP700 and STARBON-800 was active in the photocatalytic oxidation of methanol in gas phase (see SI, Table S1). The results showed that the best ultrasound amplitude used during the synthesis was 48 µm with pulse mode and the best loading of TiO_2 used during the synthesis was 20.4 wt. %TiO_2 for TiO_2/STARBON-800 and TiO_2/SWP700. It should be noted that the 20.4 wt. %TiO_2/STARBON-800_48 µm (UV light: 33.8%, visible light: 3.2%) and 20.4 wt. %TiO_2/SWP700_48 µm (UV light: 29.3%, visible light: 4.3%) photocatalysts exhibited the highest methanol conversion and 100% CO_2 as the only one mineralization product after 240 minutes of illumination (Fig. 8). It is also worth stressing that all materials that have been tested in different control conditions (see SI, Table S1) to obtain the crystalline form of TiO_2 embedded on carbon materials, 20.4 wt. %TiO_2/NORIT_48 µm and TiO_2_48 µm have proved to be inactive in the photocatalytic methanol oxidation under UV and visible light.
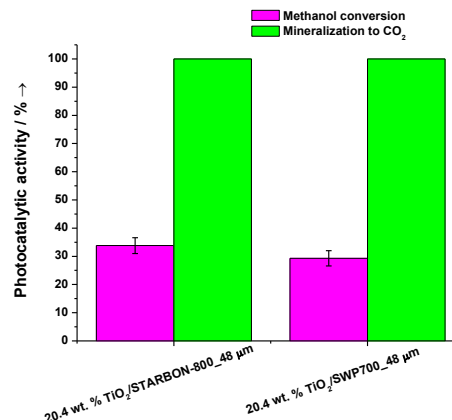
Figure 8. Photocatalytic oxidation of methanol under UV light of 20.4 wt. % TiO_2/STARBON-800_48 µm and 20.4 wt. %TiO_2/SWP700_48 µm after optimization (error bars showing the mean deviation of three experimental results)

Long-term stability test

The results of the catalytic long-run stability tests are shown in Fig. 9. It should be emphasized that 20.4 wt.% TiO_2/STARBON-800_48 µm and 20.4 wt. %TiO_2/SWP700_48 µm be tested five times under the same reaction conditions with

the loss of only < 4 % of photocatalytic methanol conversion after run 5 (20 h of illumination).
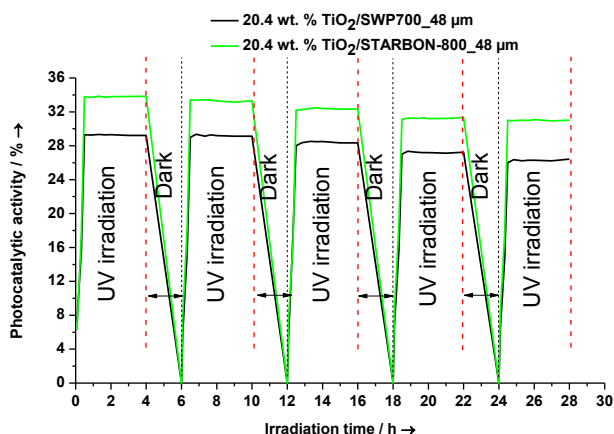

Figure 9. Photocatalytic activity of 20.4 wt. %TiO$_2$/STARBON-800 and 20.4 wt. %TiO$_2$/SWP700 sonicated at 48 μm ultrasound amplitude in a long-run test of photocatalytic oxidation of methanol in gas phase under UV light illumination

Proposed plausible mechanism for the formation of crystalline TiO$_2$ on lignocellulosic carbon materials prepared *via* ultrasound-assisted sol-gel method

FT-IR spectroscopy and HR-XPS were employed to identify the plausible mechanism for the formation of 20.4 wt. % TiO$_2$/SWP700_48 μm (Fig. 10), 20.4 wt. %TiO$_2$/STARBON-800_48 μm (Fig. 11) and 20.4 wt. %TiO$_2$/NORIT_48 μm (SI, Fig. S13) *via* ultrasound-assisted sol-gel method (Fig. 12). After each preparation stage the material was filtered and dried at 110 ^{o}C for 5h, and then analyzed by FT-IR spectroscopy and HR-XPS. Comparing pure carbon materials (SWP700, STARBON-800 and NORIT) with materials after Stage I (Table 3 and 4) we can conclude that ultrasound waves can be used to stimulate the formation of surface functional groups such as C-C sp^2 and sp^3, C-O-C, COOH, O=C-O and C=C-OH that may be activated during the Stage I. The formation of new functional groups (COOH, O=C-O and C=C-OH) on the surface of SWP700 was also observed in our previous study[35] where these functional groups favored a better interaction between TiO$_2$ precursor and SWP700 surface. Generally, it may be noted that ultrasound can cause an increase of the surface activity of all carbon functional groups present on the surface of SWP700 and STARBON-800 (Table 3 and 4). After the Stage II, it can be seen the initial step of formation of characteristic cross-linking bonds between lignocellulosic carbon materials and citric acid as previously reported,[12-20] and also confirmed, in this work by HR-XPS measurements, the presence of C=O (~ 531.2 eV) and C-O (~ 533.1 eV) on the surface of SWP700 and STARBON-800 which visibility increase further with the treatment steps (Table 3 and 4).
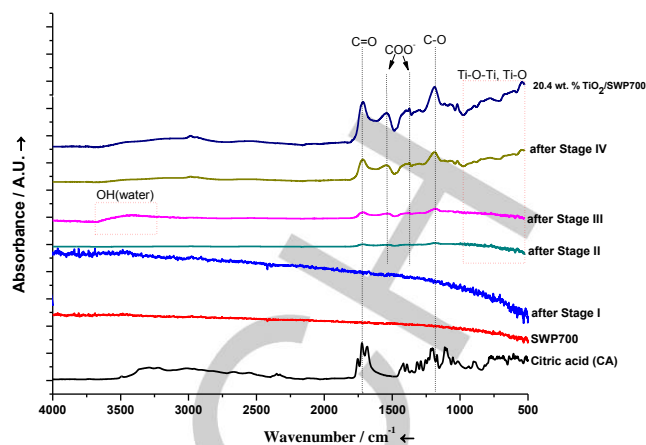
Figure 10. FTIR spectra of pure Citric acid (CA), SWP700, and materials from individual stages of 20.4 wt. %TiO$_2$/SWP700 synthesis (ultrasound amplitude = 48 μm)
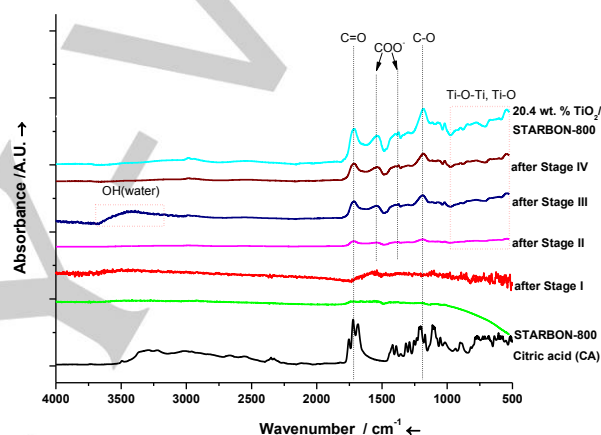
Figure 11. FTIR spectra of pure Citric acid (CA), STARBON-800, and materials from individual stages of 20.4 wt. %TiO$_2$/STARBON-800 synthesis (ultrasound amplitude = 48 μm)
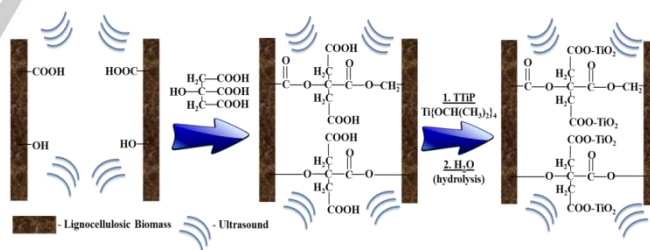
Figure 12. Schematic diagram for the plausible formation of crystalline TiO$_2$ on lignocellulosic carbon materials prepared *via* ultrasound-assisted sol-gel method

Bands observed in the 1700-1730 cm^{-1} and 1160-1200 cm^{-1} regions (Fig. 10 and 11) are assigned to C=O and C–O stretching modes (these groups are also ubiquitous for lignocellulosic carbon materials derived from biomass like starch[15] and wood[19]). These are believed to be the esteric and etheric groups[12-20] formed from the reaction between the carboxylic and hydroxylic group of CA and lignocellulosic carbon materials surface (Fig. 10 and 11, FTIR results). In this process,

free radicals obtained on citric acid can directly bind to carbon material (with -OH and -COOH functional groups) free radicals producing esteric and etheric cross-linkages. Since the prepared materials were cleaned to remove the unbound citric acid and impurities, the presence of these peaks confirms the chemical interaction between CA and carbon materials surface. Additionally, in Stage II, Ti precursor (TTiP) was added during the synthesis, and its cations were observed in the case of 20.4 wt.% TiO_2/SWP700_48 µm and 20.4 wt. %TiO_2/STARBON-800_48 µm (Table 3 and 4) by the presence of small at. % of Ti^{4+} and Ti^{3+} which surface concentration increase further with the treatment steps. It is well known that low frequencies ultrasound may induce oxygen vacancies and Ti^{3+} which may be responsible for morphological, optical and surface changes in the prepared composite materials and may also help to control the course of sonocrystallization processes. In Stage III, water was added during the synthesis, and its presence has been mainly observed in the case of 20.4 wt. %TiO_2/SWP700_48 µm (Fig. 10) and 20.4 wt. %TiO_2/STARBON-800_48 µm (Fig. 11) by a characteristic broad peak in the 3200-3600 cm^{-1} region (Fig. 12). In the case of 20.4 wt. %TiO_2/NORIT_48 µm (Fig. S13), no noticeable presence of this characteristic peak was observed, possibly due to the hydrophobic nature of NORIT during the ultrasound-assisted sol-gel method. It can be stated that the addition of water promote hydrolysis and condensation reactions and finally the formation of Ti-O-Ti chains, especially under sonication conditions where the reaction rates of hydrolysis and condensation can be increased by a better mass transfer and diffusion of reagents. After stage IV, there was an increase of the signal in already existing bands and the main peak appearing in the range of 450-550 cm^{-1} corresponds to Ti–O vibration.[34, 36] Additionally, the FT-IR bands in 700-900 cm^{-1} pointed out Ti-O-Ti bond in the TiO_2 anatase phase.[30-36] Increase in the intensity of these bands was also attributed to the successful formation of titania nanoparticles on the lignocellulosic carbon surface. It is also worth noting that two prominent bands in 1530-1570 and 1350-1400 cm^{-1} regions are assigned to the asymmetric $v_a(COO^-)$ and symmetric $v_s(COO^-)$ stretching of the carboxylate group (Fig. 10 and 11). Recent research[36] has suggested that free carboxylate anions of the crosslinked citric acid have high affinity towards the positive charges of Ti^{4+} leading to the electrostatic linkages. The last stage of the synthesis (aging-72h) is also crucial because the structural rearrangement of the gel network takes place, increasing the degree of crystallization of TiO_2 as confirmed by control experiments (see SI, Fig. S1-S5). Compared to STARBON-800 and SWP700, the peak intensity of C=O and C-O was lower in the case of NORIT. This observation illustrates that the chemical interaction occurred more easily between the STARBON-800 / SWP700 and CA than that between NORIT and CA. Thus, part of the acid may not have been "available" for the formation of crosslinking with the NORIT which in turn results in the absence of the crystalline TiO_2 on its surface.

Table 3. HR XPS results for TiO_2/SWP700 composite material prepared by ultrasound-assisted sol-gel method

		Materials						
		SWP700 PURE	Stage I	Citric Acid	Stage II	Stage III	Stage IV	TiO₂/ SWP700
C 1s BE eV (at %)	C-C sp²	283.8 (84.3)	284.1 (80.11)	284.2 (6.53)	284.1 (60.5)	284.1 (43.6)	284.1 (33.9)	283.9 (14.74)
	C-C sp³	284.8 (6.05)	285.1 (7.97)	285.1 (15.27)	285.0 (9.18)	285.1 (7.80)	285.0 (6.93)	284.9 (3.04)
	C-O-C	285.9 (1.97)	285.4 (3.32)	285.5 (5.72)	285.4 (3.71)	285.6 (3.39)	285.5 (2.92)	285.8 (2.43)
	COOH	-	287.7 (2.50)	287.6 (3.67)	287.5 (3.19)	287.7 (4.28)	287.5 (4.75)	288.0 (6.50)
	O=C-O, C=C-OH	-	289.1 (2.61)	289.0 (18.86)	289.0 (3.48)	289.2 (4.13)	289.1 (4.28)	289.0 (4.60)
Ti 2p BE eV (at %)	Ti⁴⁺	-	-	-	460.9 (2.26)	461.0 (3.89)	461.0 (5.08)	460.7 (11.61)
	Ti³⁺	-	-	-	460.1 (0.14)	460.3 (0.40)	460.2 (0.51)	459.7 (0.89)
O 1s BE eV (at %)	Ti-O-Ti	-	-	-	529.6 (4.64)	529.7 (11.66)	529.7 (13.21)	529.7 (16.32)
	Ti-O C=O	-	-	531.2 (29.2)	531.0 (4.88)	531.2 (8.79)	531.1 (14.82)	530.7 (19.54)
	C-O, C-OH (C-O-C)	532.6 (2.37)	532.9 (2.95)	533.1 (20.31)	533.2 (6.33)	533.3 (10.98)	533.2 (12.87)	533.2 (16.27)

Table 4. HR XPS results for TiO_2/STARBON-800 composite material prepared by ultrasound-assisted sol-gel method

		Materials						
		STARBON-800 PURE	Stage I	Citric Acid	Stage II	Stage III	Stage IV	TiO₂/ STARBON-800
C 1s BE eV (at %)	C-C sp²	284.2 (69.66)	284.1 (71.90)	284.3 (6.53)	283.9 (37.75)	284.0 (33.89)	284.1 (29.71)	284.1 (21.52)
	C-C sp³	284.7 (14.97)	285.2 (15.42)	285.1 (15.27)	285.0 (21.83)	285.1 (20.28)	285.1 (19.52)	284.8 (14.50)
	C-O-C	286.0 (2.78)	286.3 (2.97)	285.7 (5.72)	286.0 (3.73)	286.1 (3.84)	285.9 (4.50)	286.2 (4.87)
	COOH	288.2 (2.20)	287.7 (2.52)	287.8 (3.67)	287.7 (2.71)	287.6 (3.04)	287.9 (3.45)	288.1 (3.95)
	O=C-O, C=C-OH	288.8 (2.02)	289.1 (3.30)	289.0 (18.86)	289.1 (6.52)	289.3 (5.26)	289.4 (4.80)	288.9 (2.74)
Ti 2p BE eV (at %)	Ti⁴⁺	-	-	-	461.0 (3.93)	461.0 (4.45)	461.1 (5.11)	460.9 (12.22)
	Ti³⁺	-	-	-	460.4 (0.24)	460.6 (0.48)	460.4 (0.52)	459.9 (0.94)
O 1s BE eV (at %)	Ti-O-Ti	-	-	-	530.1 (7.96)	530.4 (11.75)	530.0 (13.21)	530.3 (18.07)
	Ti-O C=O	-	-	531.2 (29.2)	531.2 (10.59)	531.1 (11.39)	531.3 (12.83)	530.9 (13.7)
	C-O, C-OH (C-O-C)	532.3 (2.79)	533.4 (3.57)	533.1 (20.31)	533.2 (4.20)	533.2 (4.94)	533.3 (5.82)	533.1 (6.54)

Conclusions

A novel low temperature ultrasound-induced green approach for TiO_2 sonocrystallization on lignocellulosic carbon materials (STARBON-800 and SWP700) has been reported. Compared with conventional methods, the main advantages of the present method are milder and greener reaction conditions, simple methodology and elimination of the high-temperature treatment step (material calcination) required in the conventional sol-gel method for the preparation of similar metal oxide nanostructures. The best performing 20.4 wt. % TiO_2/STARBON-800_48 µm and 20.4 wt. %TiO_2/SWP700_48 µm photocatalysts exhibited favorable properties, such as 100% anatase nanoparticles, high surface area (517 m^2g^{-1} and 242 m^2g^{-1}, respectively), and promising photocatalytic activity and stability (without Ti leaching) in liquid (phenol mineralization) and gas (methanol mineralization) phase, especially under near UV light. Ultrasound in this method can stimulates surface functional groups formation such as C-C sp^2 and sp^3, C-O-C, COOH, O=C-O and C=C-OH (confirmed by HR-XPS) and may lead to the evolution of surface oxygen vacancies and Ti^{3+} defects which could be responsible for morphological, optical and surface changes in the prepared composite materials and also help to control the course of sonocrystallization processes. Citric acid as a cross-linking agent showed, under ultrasound treatment, to improve significantly TiO_2 complexation, segregation and crystallization on the surface of lignocellulosic carbon materials.

To sum up, this proof of concept possesses a very high degree of novelty and should open new opportunities to develop more innovative eco-friendly, sustainable and efficient methodologies for the synthesis of nanostructured composite materials.

Experimental Section

Preparation of composite TiO₂-based carbon materials

Titanium (IV) isopropoxide (TTIP > 98%, Acros organics) was used as a precursor of titanium dioxide. Carbon materials: NORIT (activated carbon NORIT SX 2, CAS: 7440-44-0, POCH), SWP700 (Soft Wood Pellets pyrolyzed at 700 °C), STARBON® (STARBON-800, CAS: 1333-86-4, Sigma-Aldrich). The SWP700 used in this study belong to the so-called Edinburgh Standard Biochar set (www.biochar.ac.uk/standard) and was produced using the UKBRC Stage III Pyrolysis Unit (rotary kiln pyrolyser) at the University of Edinburgh.[35] Crystalline TiO₂/carbon material composites were prepared by a novel green ultrasound-assisted sol-gel method.[37] The typical preparation procedure of the crystalline TiO₂/carbon material composites was as follows: first, carbon materials were washed thoroughly three times in boiling Milli-Q water and subsequently dried in an oven at 110 °C overnight. The preparation of 20.4 wt. %TiO₂-based carbon materials (SWP700, NORIT, STARBON-800), sonicated at 48 μm of amplitude, was conducted as depicted in Fig. 13. Prior to the synthesis, 0.5 g of carbon material with 100 mL of isopropanol (99.7 %, POCH, CAS: 67-63-0) were transferred into a sonoreactor and sonicated (QSonica 700, 20 kHz, 700 W) for 0.5 h and kept for 24 h (stage I). Then, 335.6 mg of citric acid (CA) (Monohydrate, CAS: 5949-29-1) (after optimization total molar ratio of CA:TTIP was 1:1) was dissolved in 20 mL of isopropanol and poured into a termostated (5 °C) sonoreactor and subsequently, the reaction mixture (0.5 mL of TTIP (1.6 mmol) in 10 mL of isopropanol) was added dropwise *via* a syringe pump (0.5 mL min⁻¹, New Era Syringe Pump NE-1000) with simultaneous sonication for 10 min. in a 5 s pulse mode i.e. 5 s ON and 5 s OFF mode (stage II). The mixture thus obtained, after keeping it for 24 h, was again ultrasonically irradiated while keeping the same parameters of preparation and adding 17.5 mL of Milli-Q water (total volume ratio of H₂O:TTiP was 35:1) by a syringe pump (0.5 mL min⁻¹) (stage III). The mixture thus obtained, after kept for 24 h, was subjected to sonication again with the same conditions of ultrasound but different temperature (50 °C) of termostated sonoreactor (stage IV). After the ultrasound treatment, the mixture was aging for 72 h and then filtered and dried at 110 °C for 5 h in an oven, and finally, the crystalline TiO₂/carbon material composites were gathered in a container within desiccator for characterization and photocatalytic test reactions. For the sake of comparison, composite materials were prepared under different reaction conditions (see Supplementary Information (SI), Fig. S1-S5) to confirm the crystalline phase of TiO₂ in the experimental setup shown in Fig. 13. Following rational selection process of photocatalytic test reactions in water and gas phase (see SI, Fig. S6-S11 and Table S1), 20.4 wt. % loading of TiO₂ on carbon materials sonicated at 48 μm was selected and studied by a spectrum of physicochemical techniques. For comparative purposes (see SI, Table S1), pure carbon materials (STARBON-800, SWP700 and NORIT), 20.4 wt. %TiO₂/NORIT and precursor of titanium dioxide (TTiP) sonicated at 48 μm of amplitude were prepared.
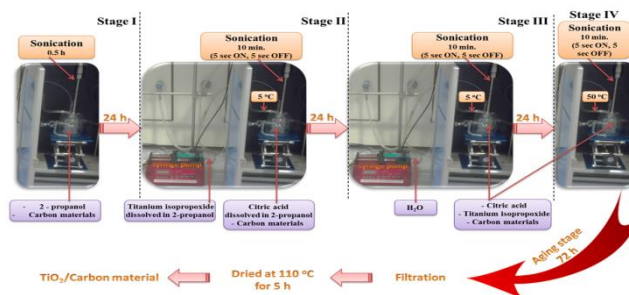

Figure 13. Synthesis procedure for composite TiO₂/carbon materials using ultrasound-assisted sol-gel method [37]

Photocatalysts activities in aqueous phase

All catalytic reactions were performed in a Pyrex cylindrical double-walled immersion well photoreactor. The bath photoreactor was stirred magnetically to obtain a homogenous suspension of the catalyst. A medium pressure 125 W mercury lamp (λmax = 365 nm), supplied by Photochemical Reactors Ltd. UK (Model RQ 3010) was placed inside the glass immersion well as light irradiation source. The reaction temperature was set at 30 °C. Phenol solution (99%, CAS: 108-95-2) of 50 mg L⁻¹ was prepared in Milli-Q water. Before the photocatalytic reaction, the prepared suspension was stirred in the dark for 120 min to reach the adsorption/desorption equilibrium. After dark adsorption procedure, the suspension was irradiated. Samples were taken out (see Fig. 6-9) at regular time intervals, and they were immediately stored in a 2.0 mL screw cap glass. Photocatalytic degradation under visible light was investigated in a glass reactor (V=20 mL) using sun-imitating super-quiet Xenon lamp (150 W, L2195 Hamamatsu, 240-2000 nm) with UV/IR-Cut filter (BAADER, blocks UV below 400 nm and IR above 680 nm). The average luminous intensity for UV light (220-400 nm, 265.0 ± 1.6 W m⁻²) and visible light (distance between lamp and photoreactor: 8 cm, 400-680 nm, 61.0 ± 1.4 W m⁻²) was examined by radiometer HD2302.0 (Delta Ohm, Italy). At each sampling point, approx. 1 mL sample was periodically taken from the photoreactor and filtered through 0.2 μm, 25 mm nylon filters to remove photocatalyst.

Phenol degradation was measured, after external standard calibration, by a high-performance liquid chromatography HPLC (2998 Photodiode Array (PDA) Detector, Sample Manager FTN-R and Quaternary Solvent Manager supplied by Waters). Separation was performed on an XBridgeTM C18, 5 μm, 4.6 mm x 150 mm column provided by Waters. The mobile phase consisted of Milli-Q water-methanol (Super Gradient, CAS: 67-56-1) (65:35 v/v) mixture with 0.1% of CF₃COOH (Trifluoroacetic acid, 99.9 %, ROTH, CAS: 76-05-1) at a flow rate of 1 mL min⁻¹. The injection volume was 10 μL. Blank experiments were performed in the dark as well as with illumination and no catalyst, without an observable change in the initial concentration of phenol in both cases.

Photocatalytic activity in gas phase

The schematic representation of gas phase methanol photooxidation setup is shown elsewhere.[35] After achieving reagent–photocatalyst adsorption equilibrium in the dark (after 2 h), liquid methanol (Super Gradient, CAS: 67-56-1) was fed into glass evaporator (filled with glass beads) by a programmable syringe pump (New Era Syringe Pump NE-1000) at a constant flow rate of 1.5 μL min⁻¹. The pure synthetic air was used as a source of oxygen. The whole reactor system lines were heated to prevent condensation. This gas mixture containing 0.9 vol. % of methanol and 99.1 vol. % of air was supplied at a flow rate of

25 cm^3 min^{-1} into the photoreactor. The gas flow rates were measured and controlled by mass flow controllers (supplied by Bronkhorst HI-TEC). An aluminium foil cylindrical reflector vertically enclosed the continuous fixed-bed photoreactor (20 cm x 13 cm x 1 mm) to exclude any external light source and maximize light energy usage within the reactor. The light source was a medium pressure 125 W mercury lamp (λ_{max} = 365 nm), supplied by Photochemical Reactors Ltd. UK (Model RQ 3010) and sun-imitating Xenon lamp (150 W, L2195 Hamamatsu, 240-2000 nm) with UV/IR-Cut filter (BAADER, blocks UV below 400 nm and IR above 680 nm) built into a lamp housing and centered vertically in the reflector (2.5 cm between the lamp and photoreactor) and thermostated at 30 ^{o}C. The average luminous intensity for UV light (220-400 nm, 275±1.5 W m^{-2}) and visible light (400-680 nm, 272 ±1.3 W m^{-2}) was determined using a radiometer HD2302.0 (supplied by Delta Ohm, Italy). Reaction products were quantitatively analyzed by means of online gas chromatography (HP 5890 series II Hewlett Packard USA equipped with a flame ionization detector (FID) and a methanizer model 510 instrument supplied by SRI INSTRUMENTS) and identified offline by GC–MS (HP-5 column GC (6890 Series)–MS(5973) Hewlett Packard equipped with FID.

Materials characterization and measurements

The specific surface area, pore volume, and average pore diameter were determined by N$_2$ physisorption using a Micromeritics ASAP 2020 automated system and the Brunauer-Emmett-Teller (BET) surface area analysis and Barrett-Joyner-Halenda (BJH) pore size and volume analysis.[38] Each photocatalyst was degassed under vacuum at <1×10^{-5} bar in the Micromeritics system at 110 ^{o}C for 4 h prior to N$_2$ physisorption.

Powder XRD measurements were performed using standard Bragg–Brentano configuration. This type of arrangement was provided using Siemens D5000 diffractometer (equipped with a horizontal goniometer) with θ–2θ geometry and Ni filtered Cu Kα radiation, powered at 40 kV and 40 mA. Data were collected in the range of 2 θ = 10–90° (some data up to 120°) with step interval of 0.02^o and counting time up to 5 s per step.

The average crystallite size (D in nm) was determined according to the Scherrer equation:[39]

$$D = \frac{k\alpha}{\beta cos\theta} \quad (1)$$

where D is the average crystallite size of the catalyst (nm), λ is the wavelength of the Cu kλ X-ray radiation (λ = 0.154056 nm), k is a coefficient usually taken as 0.94, β is the full width at half maximum (FWHM) intensity of the peak observed at 2θ (radian), and θ is the diffraction angle.

The structure characterization of provided samples was carried out with high resolution Scanning Transmission Electron Microscope (STEM, Hitachi HD-2700, 200 kV, Cs corrected) equipped with Energy Dispersive X-ray spectrometer. This is 200 kV, field emission STEM machine equipped with bright-field (BF), high-angle annular dark-field (HAADF) and secondary electrons (SE) detectors. The STEM observations allow us to obtain images providing complimentary information for the same area where BF STEM image is coupled with diffraction contrast, HAADF STEM image reveals Z-contrast coming from the atomic number and SE image providing topography information. Additionally, minor observations were performed on high resolution Scanning Electron Microscope SEM SU8230 in order to provide more information connected with carbon phase. The samples for STEM and SEM observations were prepared through dispersing powder in ethanol with using an ultrasonic bath. Then drop of suspension was deposited on copper grid covered with carbon film. After alcohol evaporation the samples were ready for analysis.

X-ray photoelectron spectroscopic (XPS) measurements were performed using the PHI 5000 VersaProbe (ULVAC-PHI) spectrometer with monochromatic Al Kα radiation (hv = 1486.6 eV) from an X-ray source operating at 100 μm spot size, 25 W and 15 kV. Both survey and high-resolution (HR) XPS spectra were collected with the hemispherical analyzer at the pass energy of 117.4 and 23.5 eV and the energy step size of 0.4 and 0.1 eV, respectively. The X-ray beam was incident at the sample surface at the angle of 45° with respect to the surface normal, and the analyzer axis was located at 45° with respect to the surface.

The CasaXPS software (version 2.3.16) was used to evaluate the XPS data. Deconvolution of all HR XPS spectra was performed using a Shirley background and a Gaussian peak shape with 30% Lorentzian character. The binding energy (BE) scale of all detected spectra was referenced by setting the BE of the aliphatic carbon peak (C-C) signal to 285.0 eV.

Fourier transform infrared (FTIR) spectra were recorded on a BRUKER TENSOR II FTIR spectrometer using conventional KBr pellets.

UV–vis Diffuse Reflectance spectroscopy was performed using a UV/VIS/NIR spectrophotometer Jasco V-570 equipped with an integrating sphere. The baseline was recorded using SpectralonTM (poly(tetrafluoroethylene)) as a reference material. The baseline was recorded using SpectralonTM (poly(tetrafluoroethylene)) as reference material. Band gap energies were calculated by analysis of the Tauc-plots resulting from the Kubelka–Munk function[40] f(R) transformation of UV–vis diffuse reflectance spectra. The function f(R) was calculated using equation (2):

$$f(R) = \frac{(1-R)^2}{2R} \quad (2)$$

The Kubelka-Munk function, [f(R)hv]$^{1/2}$, is approximated by (αhv)$^{1/2}$ where α is the absorption coefficient and hv is the photon energy. A Tauc plot is generated by plotting (αhv)$^{1/2}$ versus hv. Regarding absorption threshold, is determined according to the formula (3):[40]

$$\lambda = \frac{1240}{E_{gap}} \quad (3)$$

Acknowledgements

Conflict of interest

The authors declare no conflict of interest.

[1] a) H. Duan, D. Wang, Y. Li, *Chem. Soc. Rev.* **2015**, *44*, 5778-5792; b) G. Liu, L. Wang, H. G. Yang, H.-M. Cheng, G. Q. Lu, *J. Mater. Chem.* **2010**, *20*, 831–843; c) Y. Qu, X. Duan, *Chem. Soc. Rev.* **2013**, *42*, 2568–2580; c) X. Chen, J. Zhang, B. Zhang, S. Dong, X. Guo, X. Mu, B. Fei, *Sci Rep.* **2017**, *7*, 7362; d) S. Verma, M. N. Nadagouda, R. S. Varma, *Sci Rep.* **2017**, *7*, 13596; e) K. Zhang, X. Wang, X. Guo, T. He, Y. Feng, *J. Nanopart. Res.* **2014**, *16*, 2246.

[2] a) M. Pelaez, N. T. Nolan, S. C. Pillai, M. K. Seery, P. Falaras, A. G. Kontos, P. S. M. Dunlop, J. W. J. Hamilton, J. A. Byrne, K. O'Shea, M. H. Entezari, D. D. Dionysiou, *Appl. Catal., B* **2012**, *125*, 331–349; b) M. D. Hernandez-Alonso, F. Fresno, S. Suarez, J. M. Coronado, *Energy Environ. Sci.* **2009**, *2*, 1231–1257.

[3] a) V. Budarin, J. H. Clark, F. E. I. Deswarte, J. J. E. Hardy, A. J. Hunt, F. M. Kerton, *Chem. Commun.* **2005**, 2903-2905; b) K. Milkowski, J. H. Clark, S. Doi, *Green Chem.* **2004**, *6*, 189–190; c) V. Budarin, J. H. Clark, J. J. E. Hardy, R. Luque, K. Milkowski, S. J. Tavener, A. J. Wilson, *Angew. Chem., Int. Ed.* **2006**, *45*, 3782–3786; d) M.M. Titirici, R. J. White, N. Brun, V. L. Budarin, D. S. Su, F. del Monte, J. H. Clark, M. J. MacLachlan, *Chem. Soc. Rev.* **2015**, *44*, 250-290; e) J. C. Colmenares, P. Lisowski, D. Łomot, *RSC Adv.* **2013**, *3*, 20186-20192.

[4] a) J. C. Colmenares, R. S. Varma, P. Lisowski, *Green Chem.* **2016**, *18*, 5736-5750; b) S.-H. Kong, S.-K. Loh, R. T. Bachmann, S. A. Rahim, J. Salimon, *Renewable Sustainable Energy Rev.* **2014**, *39*, 729–739; c) S. Ren, H. Lei, L. Wang, Q. Bu, S. Chen, J. Wu, *RSC Adv.* **2014**, *4*, 10731–10737; d) J. Han, X. Wang, J. Yue, S. Gao, G. Xu, *Fuel Process. Technol.* **2014**, *122*, 98–106; e) Y. Yao, B. Gao, M. Inyang, A. R. Zimmerman, X. Cao, P. Pullammanappallil, L. Yang, *Bioresour. Technol.* **2011**, *102*, 6273–6278; f) I. Velo-Gala, J. J. Lopez-Penalver, M. Sanchez-Polo, J. Rivera-Utrilla, *Appl. Catal., B* **2013**, *142-143*, 694–704; g) J. Matos, *Top. Catal.* **2016**, *59*, 394–402; h) R. A. Shawabkeh, M. Al-Harthi, S. M. Al-Ghamdi, *Energy Sources, Part A* **2014**, *36*, 93–103.

[5] a) J. C. Colmenares, *ChemSusChem* **2014**, *7*, 1512-1527; b) P. Sathishkumar, R. V. Mangalaraja, S. Anandan, *Renew. Sust. Energ. Rev.* **2016**, *55*, 426-454; b) J. R. G. Sander, B. W. Zeiger, K. S. Suslick, *Ultrason. Sonochem.* **2014**, *21*, 1908-1915; c) Y. Yoo, C. Park, J. C. Won, S.-G. Lee, K.-Y. Choi, J. H. Lee, *Polym. Adv. Technol.* **2007**, *18*, 1015–1019; d) M. N. Patil, G.M. Gore, A. B. Pandit, *Ultrason. Sonochem.* **2008**, *15*, 177–187; e) M.D.L. de Castro, F. Priego-Capote, *Ultrason. Sonochem.* **2007**, *14*, 717-724; f) J.C. Colmenares, *J. Nanosci. Nanotechnol.* **2013**, *13*, 4787-4798.

[6] H. Xu, B.W. Zeiger, K. S. Suslick, *Chem. Soc. Rev.* **2013**, *42*, 2555-2567.

[7] a) A. E. Danks, S. R. Hall, Z. Schnepp, *Mater. Horiz.* **2016**, *3*, 91-112; b) A. Matsuda, Y. Kotani, T. Kogure, M. Tatsumisago, T. Minami, *J. Am. Ceram. Soc.* **2000**, *83*, 229–231.

[8] B. Neppolian, Q. Wang, H. Jung, H. Choi, *Ultrason. Sonochem.* **2008**, *15*, 649–658.

[9] H. Eskandarloo, A. Badiei, M. A. Behnajady, G. M. Ziarani, *Ultrason. Sonochem.* **2015**, *26*, 281–292.

[10] K. Prasad, D.V. Pinjari, A.B. Pandit, S.T. Mhaske, *Ultrason. Sonochem.* **2010**, *17*, 697–703.

[11] D.V. Pinjari, K. Prasad, P.R. Gogate, S.T. Mhaske, A.B. Pandit, *Ultrason. Sonochem.* **2015**, *23*, 185–191.

[12] a) S. M. Gawish, S. M. A. El-Ola, A. M. Ramadan, A. A. A. El-Kheir, *J. Appl. Polym. Sci.* **2012**, *123*, 3345–3353; b) J. Varshosaz, R. Alinagari, *Iran. Polym. J.* **2005**, *14*, 647-656.

[13] N. Reddy, K. Warner, Y. Yang, *Ind. Eng. Chem. Res.* **2011**, *50*, 4458–4463.

[14] a) S. M. Gawish, A. M. Ramadan, S. M. Abo El-Ola, A. A. A. El-Kheir, *Polym. Plast. Technol. Eng.* **2009**, *48*, 701–710; b) A. Nazari, M. Montazer, M. Dehghani-Zahedani, *Ind. Eng. Chem. Res.* **2013**, *52*, 1365−1371; c) M. Montazer, A. Behzadnia, M. B. Moghadam, *J. Appl. Polym. Sci.* **2012**, *125*, E356–E363; d) M. P. Gashti, A. Almasian, *Sens. Actuators, A* **2012**, *187*,1-9; e) M. Montazer, E. Pakdel, *Photochem. Photobiol.* **2010**, *86*, 255–260.

[15] a) P. G. Seligra, C. M. Jaramillo, L. Famá, S. Goyanes, *Carbohydr. Polym.* **2016**, *138*, 66–74; b) N. Reddy, Y. Yang, *Food Chem.* **2010**, *118*, 702-711; c) C. Menzel, E. Olsson, T. S. Plivelic, R. Andersson, C. Johansson, R. Kuktaite, L. Järnström, K. Koch, *Carbohydr. Polym.* **2013**, *96*, 270-276; d) E. Olsson, M. Hedenqvist, C. Johansson, L. Järnström, *Carbohydr. Polym.* **2013**, *94*, 765-772; e) E. Olsson, C. Menzel, C. Johansson, R. Andersson, K. Koch, L. Järnström, *Carbohydr. Polym.* **2013**, *98*, 1505-1513; f) L. Shen, H. Xu, L. Kong, Y. Yang, *J. Polym. Environ.* **2015**, *23*, 588–594; g) X. Ma, R. Jian, P. R. Chang, J. Yu, *Biomacromolecules* **2008**, *9*, 3314–3320.

[16] A. Abdulsamad, A. R. Oyi, A. B. Isah, I. Odidi, *Br. J. Pharm. Res.* **2015**, *6*, 22-34.

[17] a) T. Karthik, R. Rathinamoorthy, R. Murugan, *J. Ind. Text.* **2011**, *42*, 99-117; b) N. A. Ibrahim, R. Refaie, A. F. Ahmed, *J. Ind. Text.* **2010**, *40*, 1-19; c) A. Nazari, M. Montazer, A. Rashidi, M. Yazdanshenas, M. B. Moghadam, *J. Appl. Polym. Sci.* **2010**, *117*, 2740-2748; d) A. Khani, N. Talebian, *J. Coat. Technol. Res.* **2017**, *14*, 651–663.

[18] a) A.A. Okeil, *Polym. Plast. Technol. Eng.* **2008**, *47*, 174-179; b) M. G. Raucci, M. A. Alvarez-Perez, C. Demitri, D. Giugliano, V. De Benedictis, A. Sannino, L. Ambrosio, *J. Biomed. Mater. Res. A* **2015**, *103*, 2045-2056; c) C.C. Wang, C.C. Chen, *J. Appl. Polym. Sci.* **2005**, *97*, 2450-2456.

[19] a) S. B. Vukusic, D. Katovic, C. Schramm, J. Trajkovic, B. Sefc, *Holzforschung.* **2006**, *60*, 439-444; b) K. Umemura, T. Ueda, S. Kawai, *J. Wood Sci.* **2012**, *58*, 38-45.

[20] C. Q. Yang, Y. Xu, D. Wang, *Ind. Eng. Chem. Res.* **1996**, *35*, 4037-4042.

[21] a) P. C. Ribeiro, A. C. F. Melo da Costa, R. H. G. A. Kiminami, J. M. Sasaki, H. L. Lira, *Mater. Res.* **2013**, *16*, 468-472; b) C.H. Chang, Y.H. Shen, *Mater. Lett.* **2006**, *60*, 129-132.

[22] H. Yin, Y. Wada, T. Kitamura, T. Sumida, Y. Hasegawa, S. Yanagida, *J. Mater. Chem.* **2002**, *12*, 378–383.

[23] F. Stevens, R. Cloots, D. Poelman, B. Vertruyen, C. Henrist, *Mater. Lett.* **2014**, *114*, 136-139.

[24] a) K.S.W. Sing, D.H. Everett, R.A.W. Haul, L. Moscou, R.A. Pierotti, J. Rouquerol, T. Siemieniewska, *Pure Appl. Chem.* **1985**, *57*, 603-619; b) Z. Hu, M. P. Srinivasan, *Microporous Mesoporous Mater.* **2001**, *43*, 267-275; c) X. Li, Y. Jiang, W. Cheng, Y. Li, X. Xu, K. Lin, *Nano-Micro Lett.* **2015**, *7*, 243-254.

WILEY-VCH

[25] T. He, X. Guo, K. Zhang, Y. Feng, X. Wang, *RSC Adv.* **2014**, *4*, 5880–5886.

[26] a) L. O. Hedges, S. Whitelam, *Soft Matter* **2012**, *8*, 8624–8635; b) S. I. Madanshetty, R. E. Apfel, *J. Am. Chem. Soc.* **1991**, *90*, 1508–1514; c) P. Qiu, W. Li, K. Kang, B. Park, W. Luo, D. Zhao, J. Khim, *J. Mater. Chem. A* **2014**, *2*, 16452–16458; d) P. Qiu, B. Thokchom, J. Choi, M. Cui, H.-D. Kim, Z. Han, D. Kim, J. Khim, *RSC Adv.* **2016**, *6*, 37434–37442.

[27] a) Q. Zhang, C. Chen, M. Wang, J. Cai, J. Xu, C. Xia, *Nanoscale Res. Lett.* **2011**, *6*, 1-7; b) T. Yordanova, P. Vasileva, I. Karadjova, D. Nihtianova, *Analyst* **2014**, *139*,1532-1540; c) X. Chen, J. Jiang, F. Yan, S. Tian, K. Li, *RSC Adv.* **2014**, *4*, 8703-8710; d) Y. Luo, J. Zhang, A. Sun, C. Chu, S. Zhou, J. Guo, T. Chen, G. Xu, *J. Mater. Chem. C* **2014**, *2*, 1990-1994.

[28] K. Eufinger, D. Poelman, H. Poelman, R. De Gryse, G.B. Marin, *Appl. Surf. Sci.* **2007**, *254*, 148–152.

[29] a) L. B. Xiong, J. L. Li, B. Yang, Y. Yu, *J. Nanomater.* **2012**, *13*, 831524-831537; b) C. P. P. Wong, C. W. Lai, K. M. Lee, S. B. A. Hamid, *Materials* **2015**, *8*, 7118-7128; c) B. Erjavec, R. Kaplan, A. Pintar, *Catal. Today* **2015**, *141*, 15-24; d) C. H. Kim, B. H. Kim, K. S. Yang, *Carbon* **2012**, *50*, 2472-2481.

[30] K. Suriye, P. Praserthdam, B. Jongsomjit, *Appl. Surf. Sci.* **2007**, *253*, 3849–3855.

[31] M. S. Hamdy, R. Amrollahi, G. Mul, *ACS Catal.* **2012**, *2*, 2641–2647.

[32] Z. Wang, C. Yang, T. Lin, H. Yin, P. Chen, D. Wan, F. Xu, F. Huang, J. Lin, X. Xie, M. Jiang, *Adv. Funct. Mater.* **2013**, *23*, 5444–5450.

[33] a) M. R. Hoffmann, S. T. Martin, W. Choi, D. W. Bahnemann, *Chem. Rev.* **1995**, *95*, 69-96; b) L. Luo, Y. Yang, M. Xiao, L. Bian, B. Yuan, Y. Liu, F. Jiang, X. Pan, *Chem. Eng. J.* **2015**, *262*, 1275-1283.

[34] a) C. Chen, M. Long, H. Zeng, W. Cai, B. Zhou, J. Zhang, Y. Wu, D. Ding, D. Wu, *J. Mol. Catal. A: Chem.* **2009**, *314*, 35-41; b) M. Keiluweit, P. S. Nico, M. G. Johnson, M. Kleber, *Environ. Sci. Technol.* **2010**, *44*, 1247-1253.

[35] P. Lisowski, J. C. Colmenares, O. Mašek, W. Lisowski, D. Lisovytskiy, A. Kamińska, D. Łomot, *ACS Sustain. Chem. Eng.* **2017**, *5*, 6274–6287.

[36] T. Hurnaus, J. Plank, *Energy Fuels* **2015**, *29*, 3601-3608.

[37] P. Lisowski, J. C. Colmenares, *Polish patent application* **2017**, P.420973.

[38] a) S. Brunauer, P.H. Emmett, E. Teller, *J. Am. Chem. Soc.* **1938**, *60*, 309-319; b) J. Li, F. Qin, L. Zhang, K. Zhang, Q. Li, Y. Lai, Z. Zhang, J. Fang, *J. Mater. Chem. A* **2014**, *2*, 13916–13922.

[39] a) B. D. Cullity, S. R. Stock, *Elements of X-ray Diffraction*, 3rd ed., Prentice HallInc., Upper Saddle River, NJ, **2001**; b) R. A. Spurr, H. Myers, *Anal. Chem.* **1957**, *29*, 760-762.

[40] H.S. Lee, C.S. Woo, B.K. Youn, S.Y. Kim, S.T. Oh, Y.E. Sung, H.I. Lee, *Top. Catal.* **2005**, *35*, 255–260.

FULL PAPER
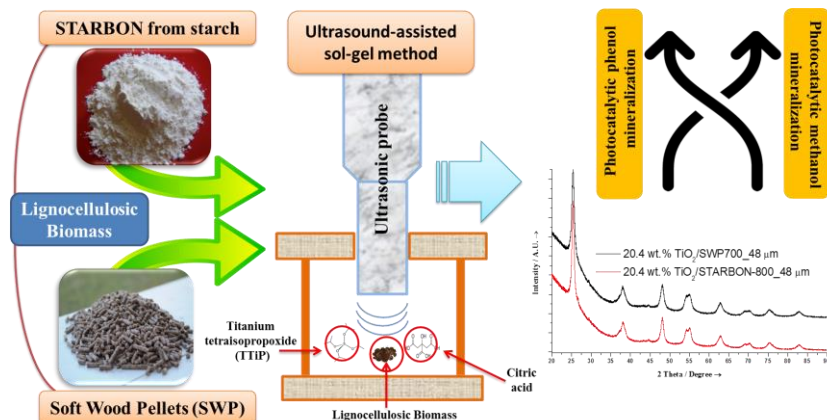
Paweł Lisowski*, Juan Carlos Colmenares*, Ondřej Mašek, Wojciech Lisowski, Dmytro Lisovytskiy, Justyna Grzonka and Krzysztof Kurzydłowski

Design and fabrication of TiO₂/lignocellulosic carbon materials: relevance of low-temperature sonocrystallization to photocatalysts performance

Immobilization of TiO_2 on lignocellulose-based carbons via low-temperature ultrasound-promoted sol-gel methodology and elimination of the high-temperature treatment step required in the conventional sol-gel method. The plausible mechanism for the formation of TiO_2 on lignocellulosic carbon materials was deeply explored.